Supplementary Information (SI) for Journal of Materials Chemistry A.

Supporting Information

Facilitating Polysulfide Conversion Kinetics via Multifunctional Solid-State Electrolytes under Lean Electrolyte Conditions for Lithium-Sulfur Batteries

*Hyunji Park[1], Jooyoung Lee[1] and Choongho Yu[1,2]**

[1] Department of Mechanical Engineering

[2] Department of Materials Science and Engineering

Texas A&M University, College Station, Texas 77843 USA

* Corresponding author: chyu@tamu.edu

Computational and Experimental Methods

Density Functional Theory (DFT) Calculations

DFT calculations were performed using the Quantum ESPRESSO code with the projector-augmented-wave (PAW) pseudopotentials. The generalized gradient approximation (GGA) of Perdew–Burke–Ernzerhof (PBE) functionals were used to implement electron exchange-correlation interactions with a kinetic energy cutoff of 400 eV. The convergence threshold for energy self-consistency was set to 1×10^{-4} eV. A Γ-point-centered Monkhorst−Pack reciprocal grid of 3×3×2 k-points was used for the first Brillouin zone sampling. To avoid interactions arising from periodic boundary conditions, a vacuum space of 20 Å was introduced in the normal direction of all the surface slabs. The maximum bonding length between lithium and sulfur is set to 3.024 Å.

Preparation of Free-Standing CNT cathodes and CNT/LGPS Cathodes

Cylindrical CNT sponges were fabricated by a chemical vapor deposition method.[1] The CNT sponges were chopped into CNT powder with a diameter of a few hundred microns with the high-energy ball miller (SPEX SamplePrep 8000M Mixer Mill). The CNT powders were mixed with polyvinylidene fluoride (PVDF, M_w ~534,000, Sigma Aldrich) at a weight ratio of 95:5 in N-methyl-2-pyrrolidinone (NMP, >99%, Sigma Aldrich) solvent. The solid concentration in NMP is 67 mg ml^{-1}. The fabricated slurry was coated on a copper substrate using a doctor blade, dried under 60 °C for 12 hours, and then punched into circular pieces (1/2 inch in diameter). To peel the CNT layer off from the substrate, the CNT layer was immersed for 10 seconds into a solution of 0.5 M $KMnO_4$ (AMRESCO, >99%) in sulfuric acid (BDH Chemicals, 95-98%) and immediately rinsed with deionized water. After a mechano-chemical acid treatment by vacuum filtration using the acid solution,[2] trenches and functional groups were generated on the surface of CNTs. The treated CNT layers were washed with deionized water at least three times, immersed in deionized water for 24 hours, and dried under 60 °C for

12 hours. LGPS is sensitive to moisture and water, so all the handling processes for LGPS were conducted in an Ar-filled glove box (with oxygen and moisture less than 0.1 ppm). LGPS powder (MSE supplies) or LLZO powder (MSE supplies) was ball milled for 10 hours with the high-energy ball miller and then sandwiched between the CNT electrodes. The thickness of a pristine CNT electrode is approximately 100-130 μm depending on the conditions, while the electrode with LGPS sandwiched and pressed measures around 180-220 μm in total. The weight ratio of CNT to sulfur is approximately 1:1, and LGPS and LLZO was optimized at 1.5 mg cm^{-2}.

Assembly and Testing of Coin Cells

The Li anodes with the artificial solid-electrolyte interphase (A-SEI) were prepared following procedure from the papers. [3, 4] The surface of thin lithium foil (Rockwood Lithium, 65 μm) was carefully polished in an Ar-filled glove box (with oxygen and moisture less than 0.1 ppm) to remove lithium oxide layers. After polishing, thin lithium foils were immersed in a solution of 0.167 M $InCl_3$ (Sigma Aldrich) and tetrahydrofuran (THF, Baker analyzed 99.8%) for 20 seconds, followed by rinsing with THF. After drying, the A-SEI-coated lithium was punched into circular pieces with a diameter of 1/2 inch. A bare electrolyte was prepared by dissolving 1M LiTFSI (Sigma Aldrich, 99%) and 0.5 M $LiNO_3$ (Alfa Aesar, 99%) in a mixture of 1,3-dioxolane (DOL) and 1,2-dimethoxyethane (DME) (Alfa Aesar, 99%) with a volume ratio of 1:1. Li_2S (Alfa Aesar, 99%) and sulfur (Alfa Aesar, 99.5%) were added to the bare electrolyte at a molar ratio of 5:1, forming a 6M electrolyte based on sulfur, referred to as the catholyte in this work. The mixture was stirred at 70 °C for 3 days under an Ar atmosphere to produce a reddish viscous catholyte solution. For assembling the Li-S cells (2032 coin cells), approximately 5 μl of bare electrolyte was applied to the A-SEI anode before covering it with a Celgard 2400 separator (5/8 inch in diameter) to ensure surface wetting. Next, around 30 μl catholyte was applied to the cathode. For cells with a lower E/S ratio of 2.9 μL mg^{-1}, 6M

catholyte was initially dropped onto the electrode, and once the solvent was completely evaporated on a hot plate, additional catholyte was added. The cells were cycled between 1.5-2.7 V for the first 2 cycles with a current density of 0.05 C to activate the batteries using an Arbin battery analyzer. All battery tests were conducted at room temperature. The C-rates were calculated based on the theoretical capacity (1675 mAh g^{-1}) of sulfur. Capacity retention was calculated based on the third cycle after two formation cycles.

Materials Characterizations

The ionic conductivity of the catholyte was measured by using a miniature dip-in conductivity probe (eDAQ ET915) at room temperature, calibrated by 0.01 M KCl solution. Scanning electron microscopy (SEM) images were obtained by a JEOL JSM-7500F field-emission scanning electron microscope. To confirm the distribution of LGPS powder and the morphology of CNTs, any remaining soluble polysulfides and lithium salts were thoroughly washed with DME solvent and then dried. UV-Vis spectra were acquired using a Hitachi U-4100 UV-Vis-NIR Spectrophotometer. Cyclic voltammetry and potentiostatic discharge experiments were conducted with an Arbin battery analyzer, while electrochemical impedance spectroscopy (EIS) analysis was performed using the Arbin battery analyzer connected with a Gamry tester. XRD patterns were obtained with a BRUKER D8 machine with a scan range (2θ) between 10º to 70º. To investigate structural changes in LGPS after cycling, we performed XRD on the electrode using a cell with approximately 4 mg of LGPS. The measurement was conducted in the discharged state, with residual polysulfides washed off with DME and the sample dried. Due to LGPS's air sensitivity, Kapton film was used during the measurement.

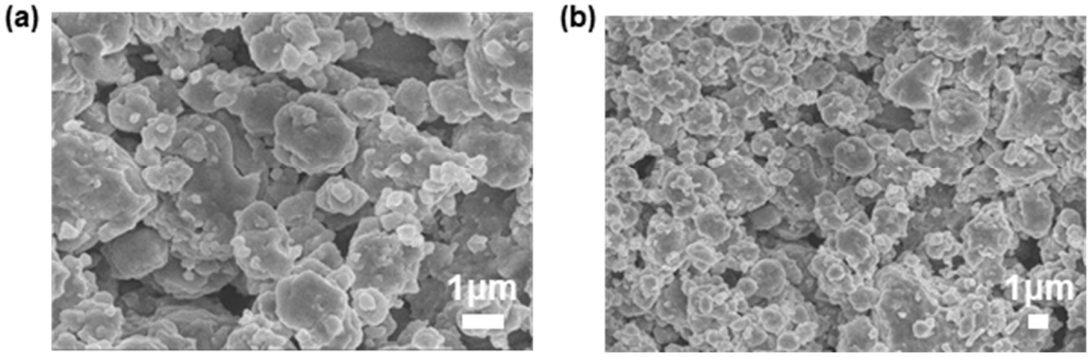

Figure S1. The SEM images of the LGPS particles.

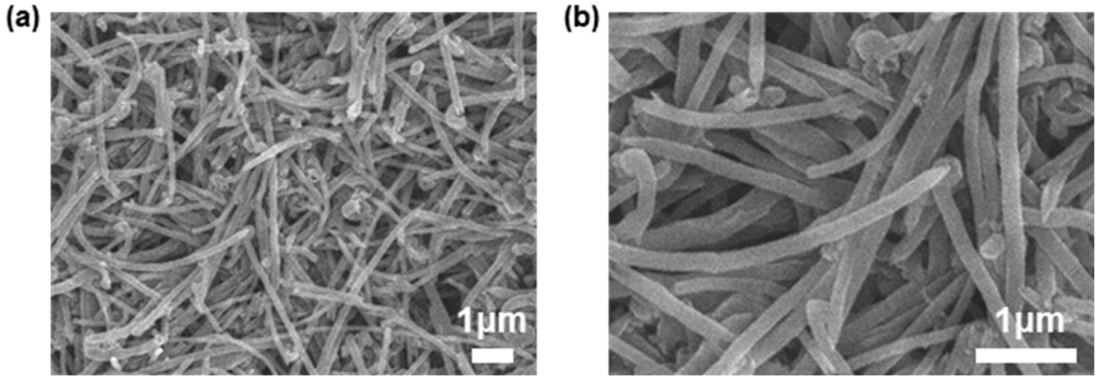

Figure S2. The SEM images of a pristine CNT/PVDF (95:5 wt%) slurry electrode.

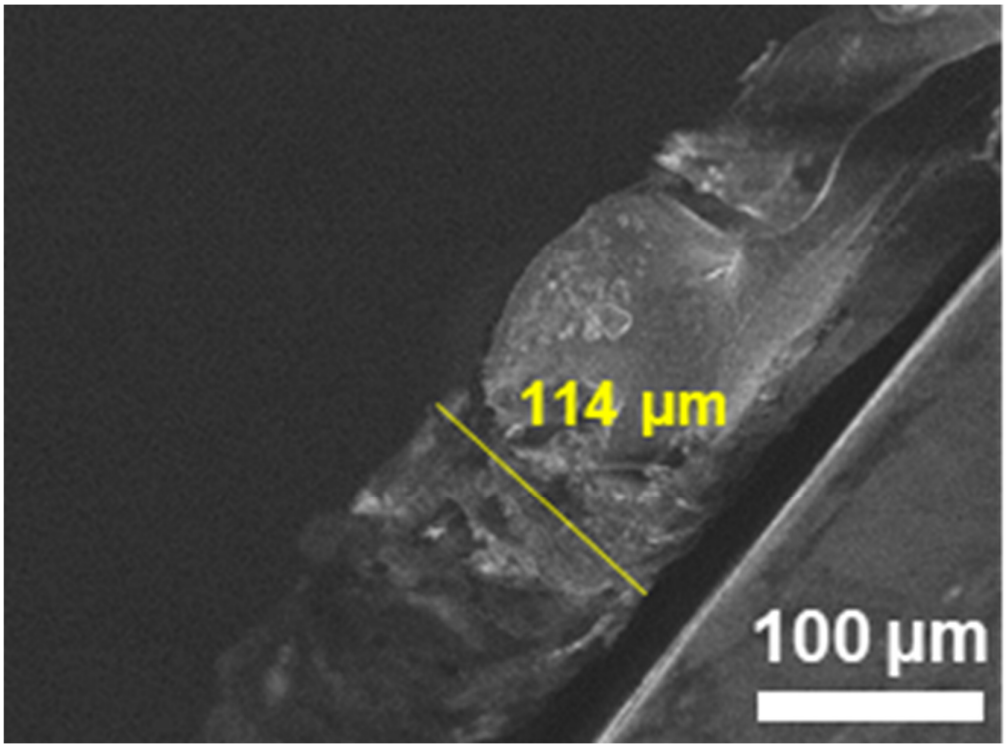

Figure S3. The cross-sectional SEM image of a CNT electrode.

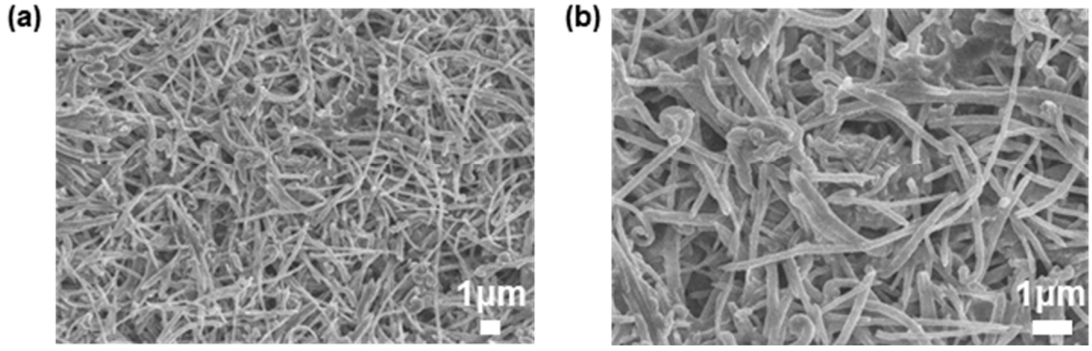

Figure S4. The SEM images of a CNT/LGPS/PVDF (6:3:1 wt%) electrode fabricated by a wet slurry coating method.

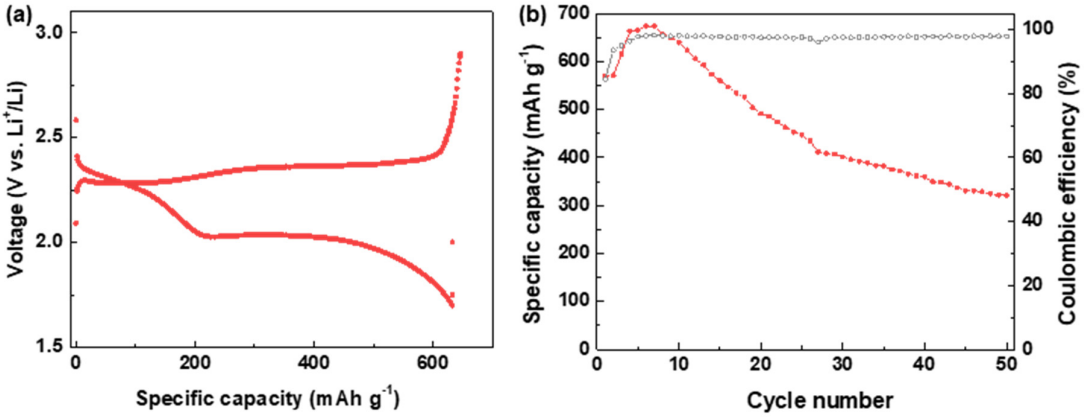

Figure S5. (a) The initial charge/discharge profile of a cell made of the wet slurry coated CNT/LGPS/PVDF (6:3:1 wt%) electrode at 0.1 C with sulfur loading of 5.7 mg cm^{-2} and E/S ratio of 4.2 µL mg^{-1}. (b) The corresponding cycling performance.

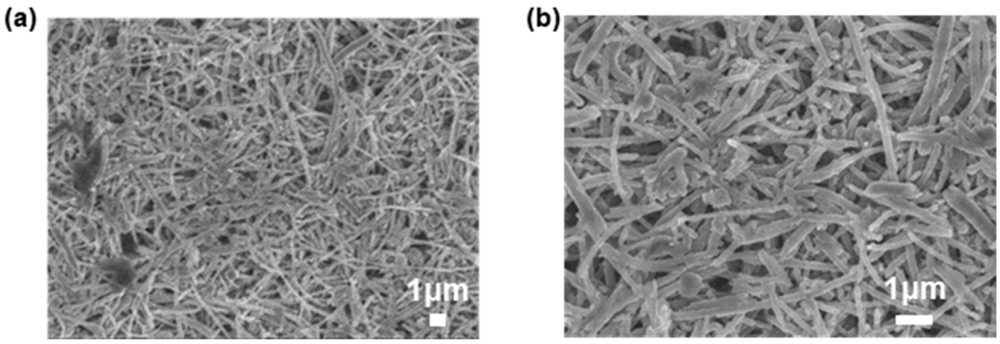

Figure S6. The SEM images of a CNT/LGPS electrode with distributed LGPS powder after cycling. The cells were tested with a sulfur loading of 4.6 mg cm^{-2} and an E/S ratio of 5.1 μL mg^{-1}. SEM was measured in the charged state (2.7 V vs. Li^{+}/Li) after two cycles of activation at 0.05 C.

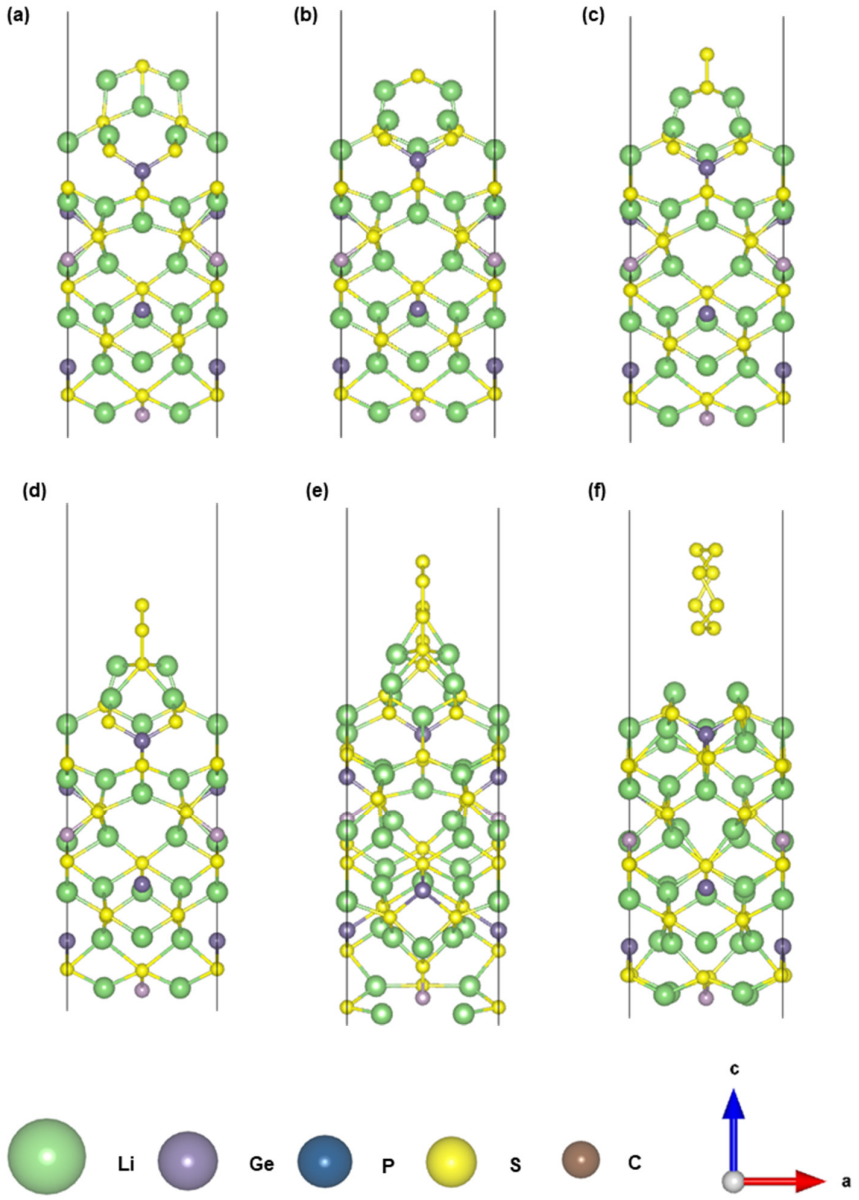

Figure S7. The optimized geometry for the adsorption of (a) Li_2S, (b) Li_2S_2, (c) Li_2S_4, (d) Li_2S_6, (e) Li_2S_8, and (f) S_8 on the LGPS (001) surface.

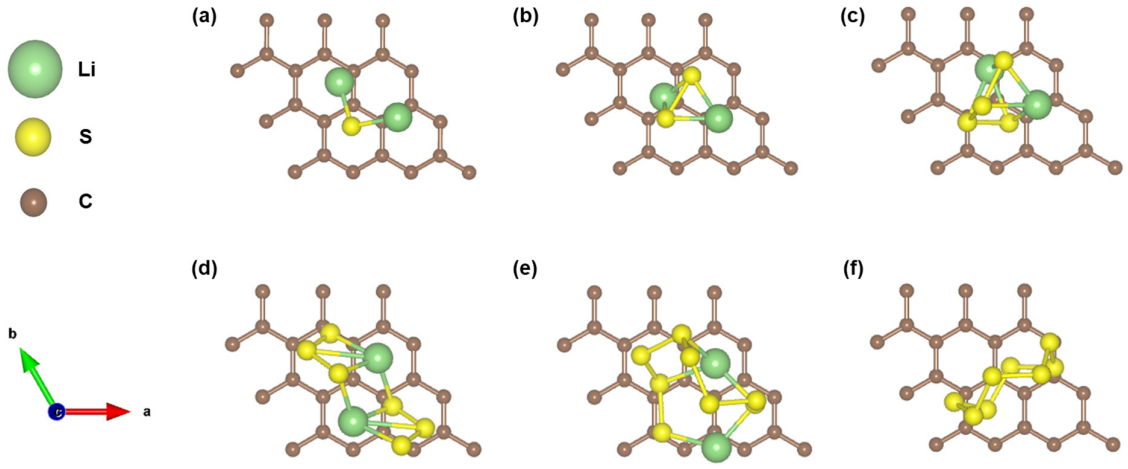

Figure S8. The optimized geometry for the adsorption of (a) Li_2S, (b) Li_2S_2, (c) Li_2S_4, (d) Li_2S_6, (e) Li_2S_8, and (f) S_8 on the surface of graphitic carbon.

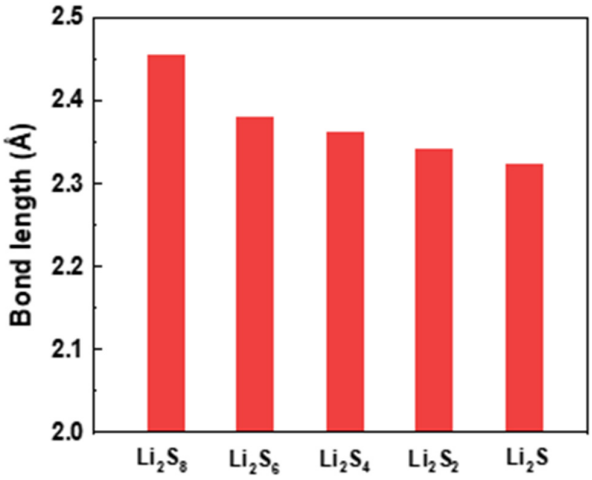

Figure S9. The shortest bond length between LGPS and polysulfide intermediates.

Table S1. The DFT results of polysulfides.

	Li_2S	Li_2S_2	Li_2S_4	Li_2S_6	Li_2S_8	S_8
Total energy [eV]	-327.8312	-607.1789	-1164.682	-1721.401	-2279.214	-2228.316

Table S2. The DFT results of LGPS (001) surface and LGPS with adsorbed polysulfides.

	LGPS (001)	LGPS- Li_2S	LGPS- Li_2S_2	LGPS- Li_2S_4	LGPS- Li_2S_6	LGPS- Li_2S_8	LGPS- S_8
Total energy [eV]	-8645.262	-8975.056	-9253.841	-9811.759	-10,367.54	-10,926.95	-10874.76

Table S3. The DFT results of graphitic carbon surface and graphitic carbon with adsorbed polysulfides.

	Graphitic carbon	Graphitic carbon- Li_2S	Graphitic carbon- Li_2S_2	Graphitic carbon- Li_2S_4	Graphitic carbon- Li_2S_6	Graphitic carbon- Li_2S_8	Graphitic carbon- S_8
Total energy [eV]	-2790.513	-3118.643	-3397.851	-3955.655	-4512.753	-5069.800	-5018.867

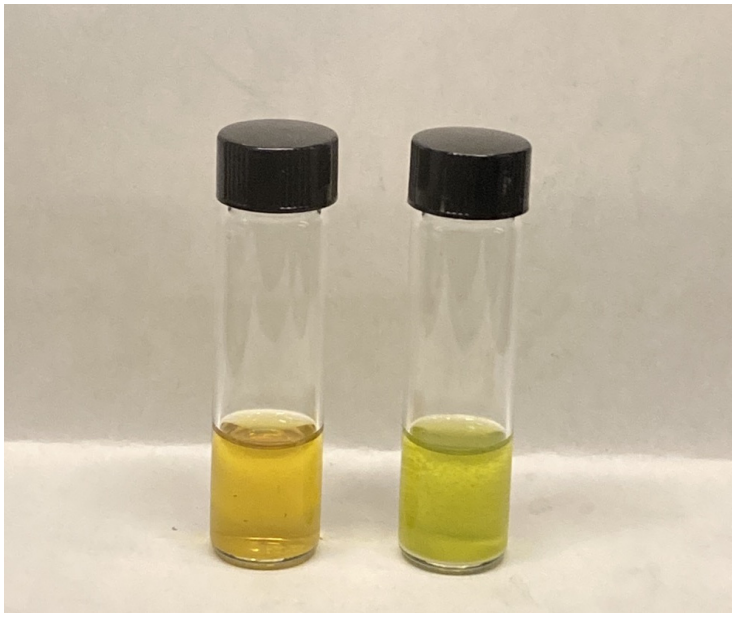

Figure S10. The photo of a 5-mM Li_2S_6 solution before (left) and after (right) immersion of LGPS in the solution.

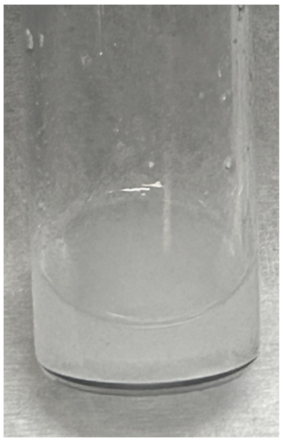

Figure S11. 10 mg of LGPS powder immersed in 1 ml of 1M LiTFSI in DOL/DME electrolyte for a day, which shows no color change due to dissolution or decomposition.

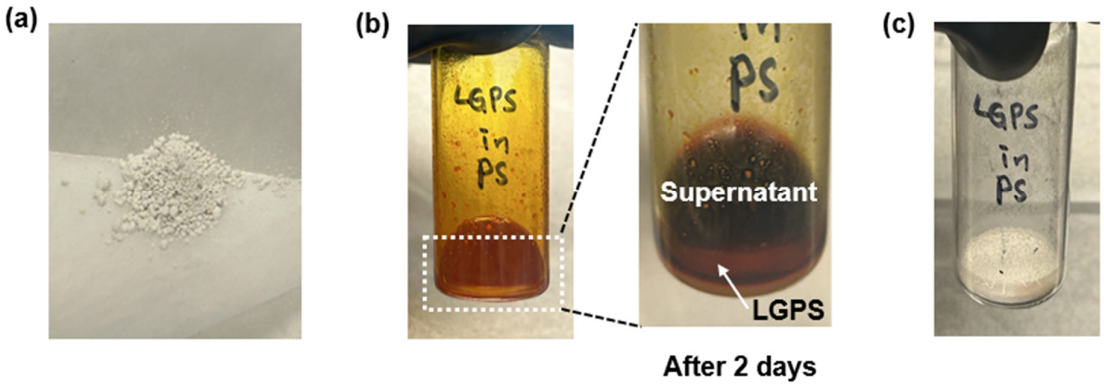

Figure S12. Images of (a) pristine LGPS powders, (b) LGPS in 6M catholyte with an enlarged view after 2 days, and (c) LGPS after washing off polysulfides.

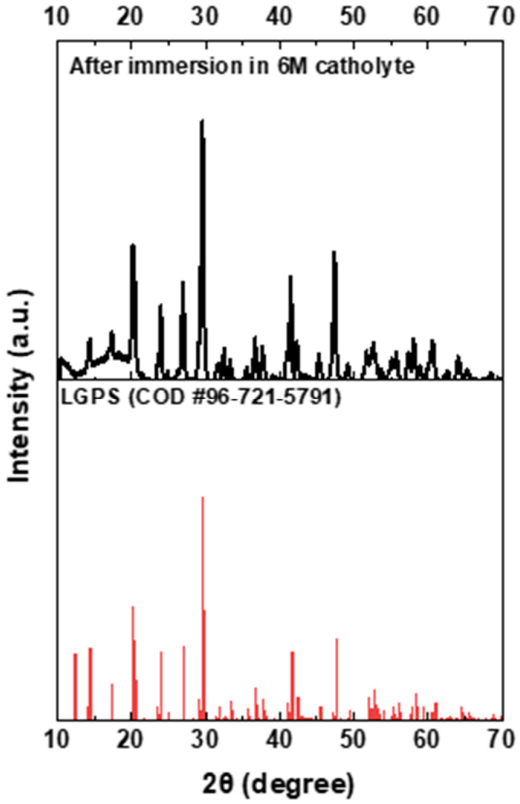

Figure S13. XRD spectra of LGPS powders after immersion in 6M catholyte.

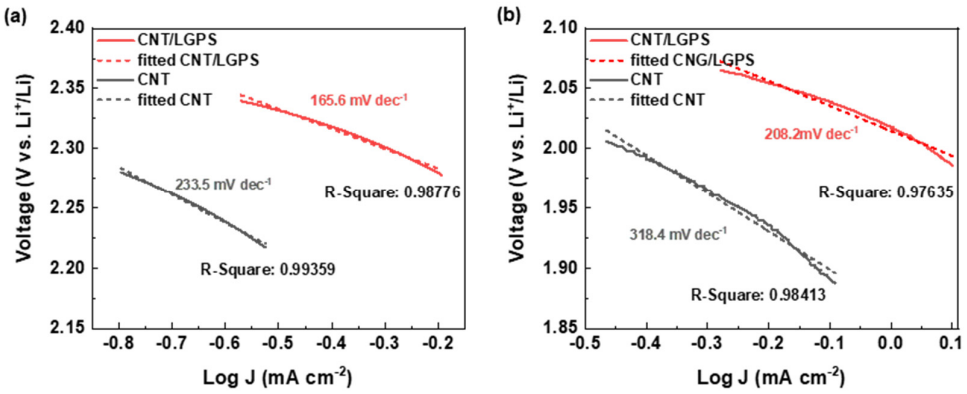

Figure S14. The fitted Tafel plots with R square values corresponding to the reductions of elemental sulfur to Li_2S_n (a) and Li_2S_n to Li_2S (b).

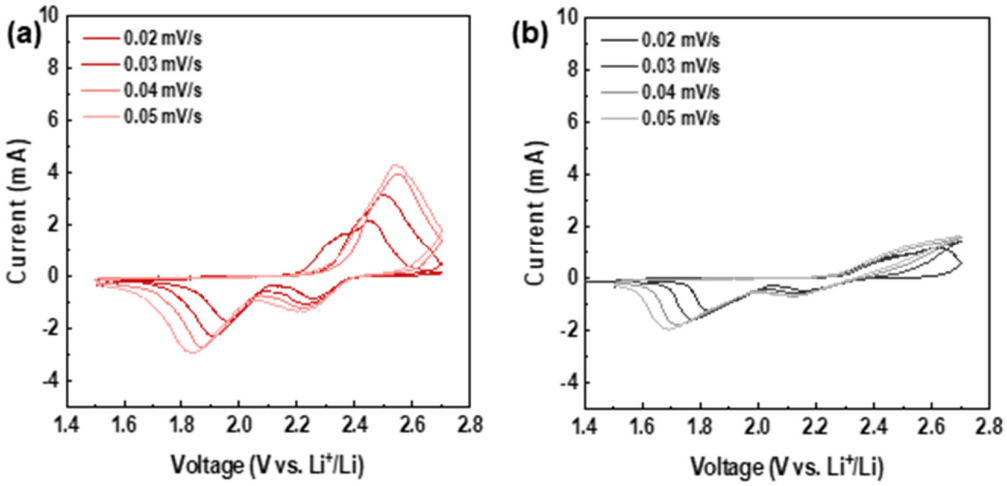

Figure S15. The cyclic voltammograms of (a) CNT/LGPS and (b) CNT. The cells were tested after activation cycles under a lean electrolyte condition (5.1 μL mg^{-1}) with a sulfur loading of 4.6 mg cm^{-1}. As the scan rate increases, two anodic peaks merge into a single peak. The highest value of the anodic peak was taken, and when calculating the diffusion coefficient, A1 and A2 were not calculated separately but were represented as a combined A.

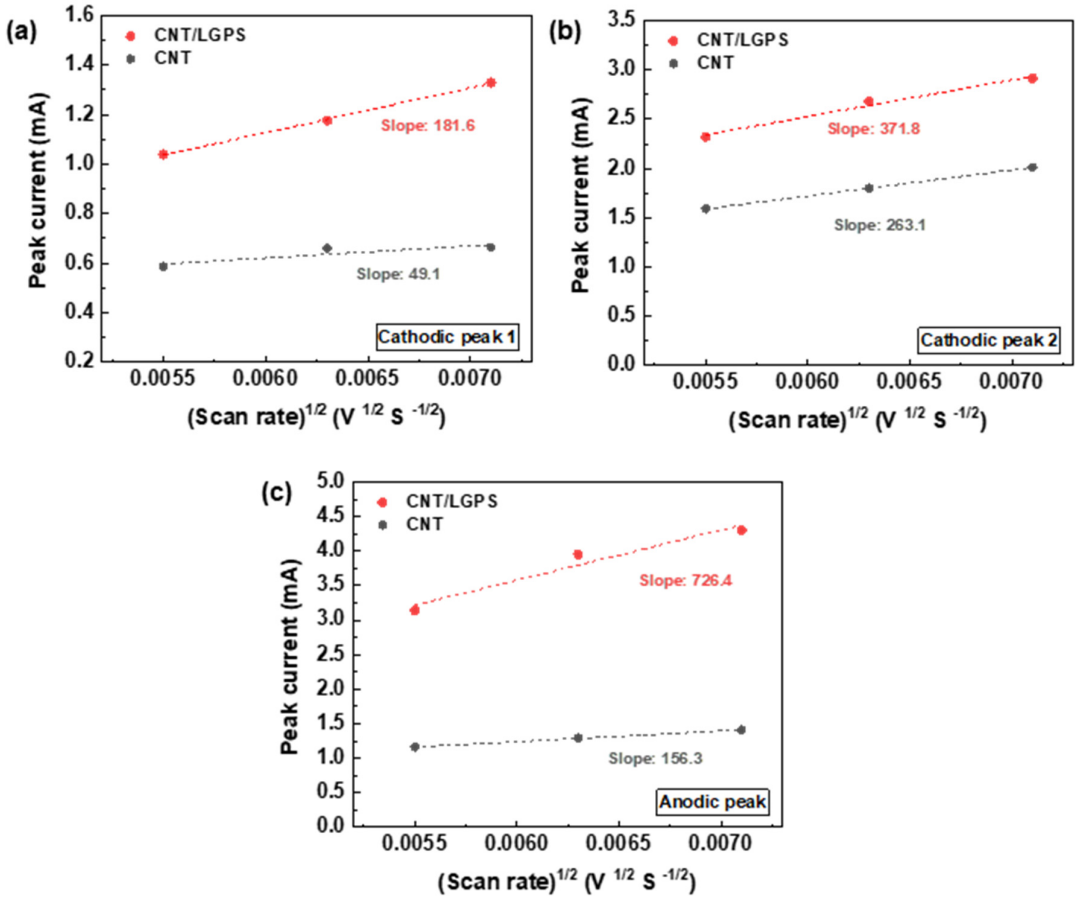

Figure S16. The plots of peak currents (i_p) with the square root of the scan rate ($v^{1/2}$) for the (a), (b) cathodic reduction processes, and (c) anodic oxidation processes. The cells were tested after activation cycles with a sulfur loading of 4.6 mg cm^{-2} and an E/S ratio of 5.1 μL mg^{-1}.

Table S4. The parameters for calculating the diffusion coefficient (D) of Li-ion using the Randles-Sevcik equation, $i_p = 0.4463nFAC\left(\frac{nFvD}{RT}\right)^{\frac{1}{2}}$, where the concentration of Li-ion (C) is 1500 mol ml^{-1}, the electrode area (A) is 1.26 cm^2, the number of electrons transferred (n) is 2, the temperature (T) is 298 K.

			Scan rate [mV/s]			R square
			0.03	0.04	0.05	
Peak current [mA]	**Cathodic peak 1**	CNT/LGPS	1.04	1.18	1.33	0.99858
		CNT	0.58	0.66	0.66	0.79284
	Cathodic peak 2	CNT/LGPS	2.32	2.68	2.91	0.98509
		CNT	1.59	1.80	2.01	0.99998
	Anodic peak	CNT/LGPS	3.14	3.95	4.30	0.95086
		CNT	1.16	1.29	1.41	0.99947

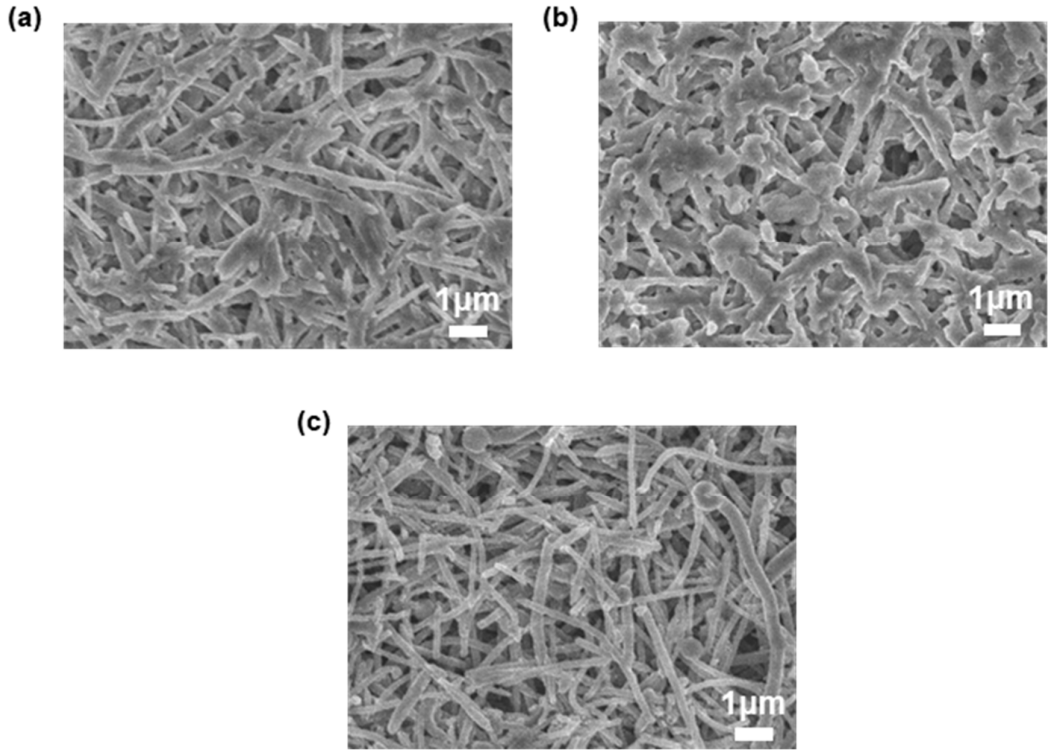

Figure S17. The SEM images of CNT/LGPS cathodes at (a) a half-discharged state (2.08 V vs. Li^+/Li), (b) a discharged state (1.5 V vs. Li^+/Li), and (c) a charged state (2.7 V vs. Li^+/Li). The cells were tested at 0.1 C with a sulfur loading of 4.6 mg cm^{-2} and an E/S ratio of 5.1 μL mg^{-1}. SEM was measured after two cycles of activation at 0.05 C.

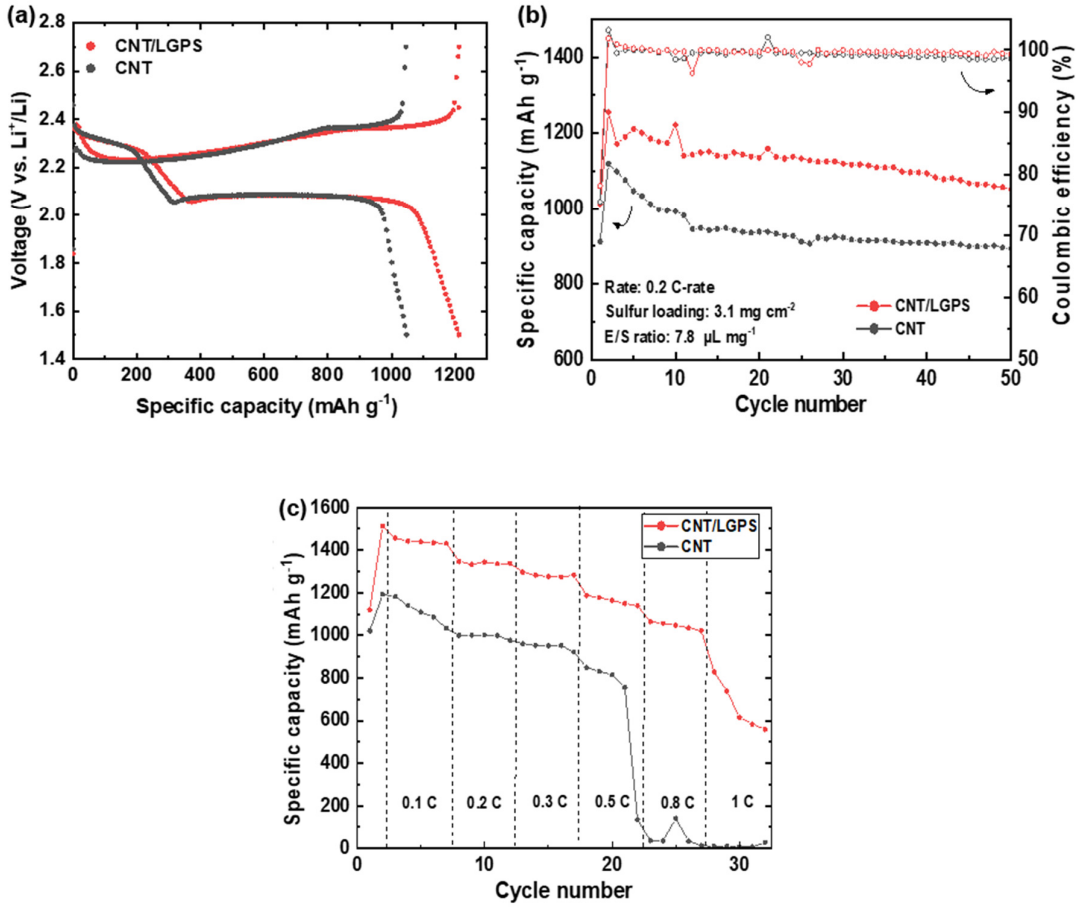

Figure S18. Electrochemical performance of Li-S cells with a sulfur loading of 3.1 mg cm^{-2} and E/S ratio of 7.8 μL mg^{-1}. (a) Representative galvanostatic charge-discharge curves of the 5th cycle at 0.2 C. (b) The cycling performance of CNT/LGPS and CNT. (c) The rate capability test of CNT/LGPS and CNT.

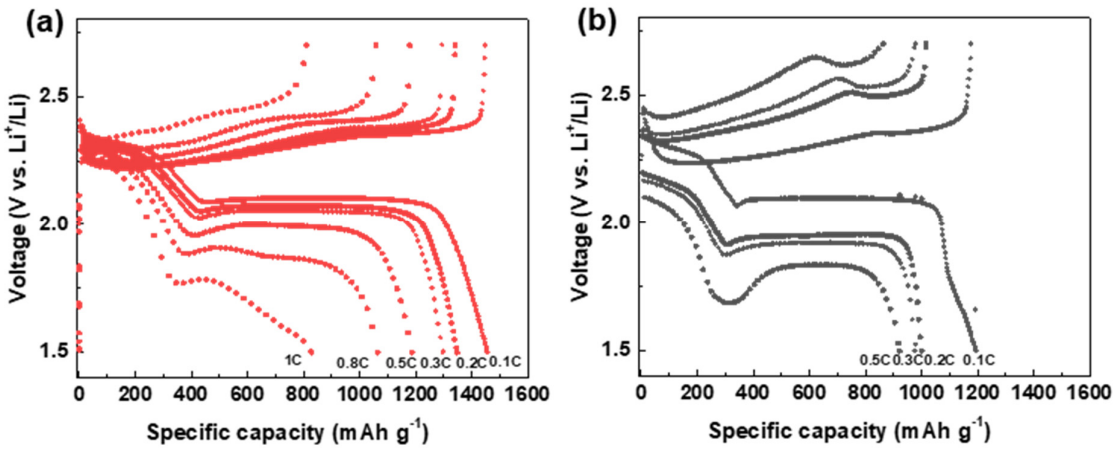

Figure S19. The representative charge/discharge profiles of (a) CNT/LGPS and (b) CNT at various rates. The cells were tested with a sulfur loading of 3.1 mg cm^{-2} and E/S ratio of 7.8 μL mg^{-1}.

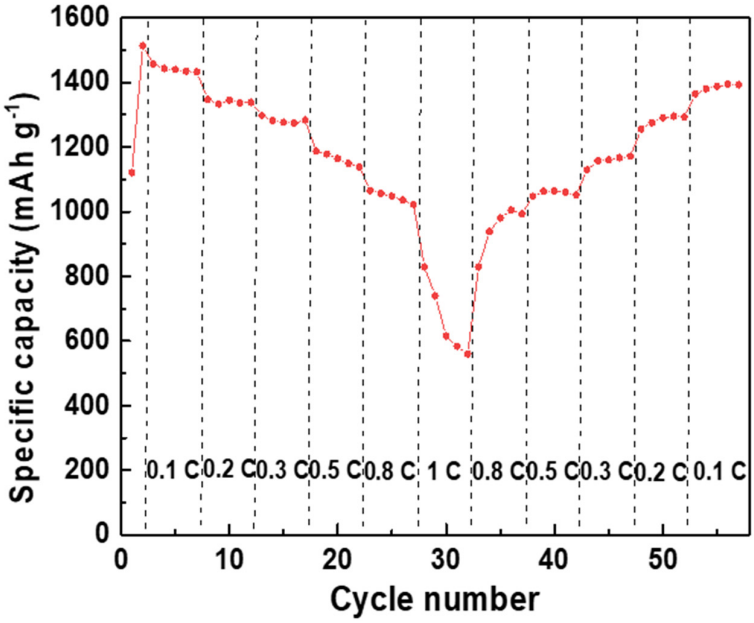

Figure S20. The rate capability of CNT/LGPS with a sulfur loading of 3.1 mg cm^{-2} and E/S ratio of 7.8 μL mg^{-1}.

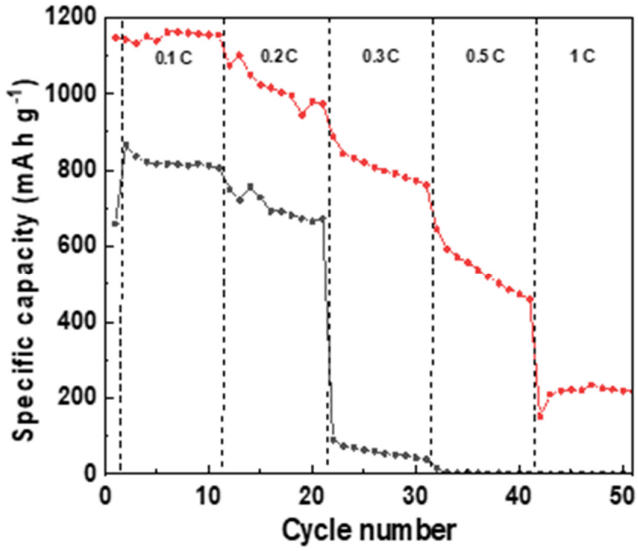

Figure S21. The rate capability of CNT/LGPS (red) and CNT (black) with a sulfur loading of 4.6 mg cm^{-2} and E/S ratio of 5.1 μL mg^{-1}.

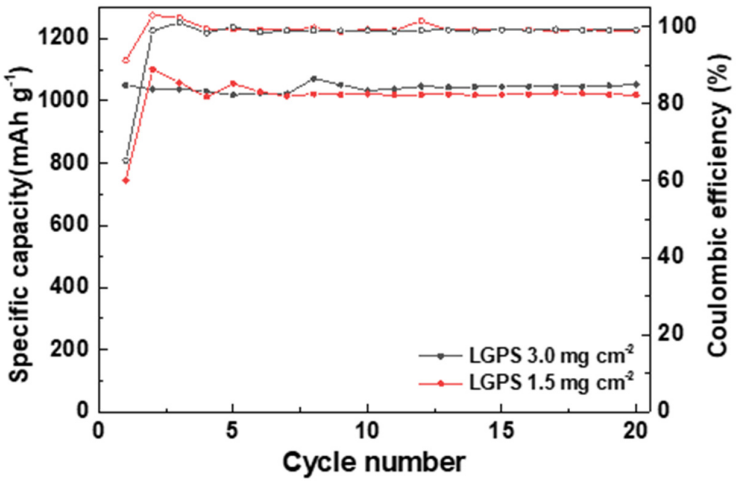

Figure S22. The comparison of CNT/LGPS with the LGPS of 1.5 mg cm^{-2} and 3.0 mg cm^{-2} at 0.1 C with a sulfur loading of 4.6 mg cm^{-2} and E/S ratio of 5.1 μL mg^{-1}.

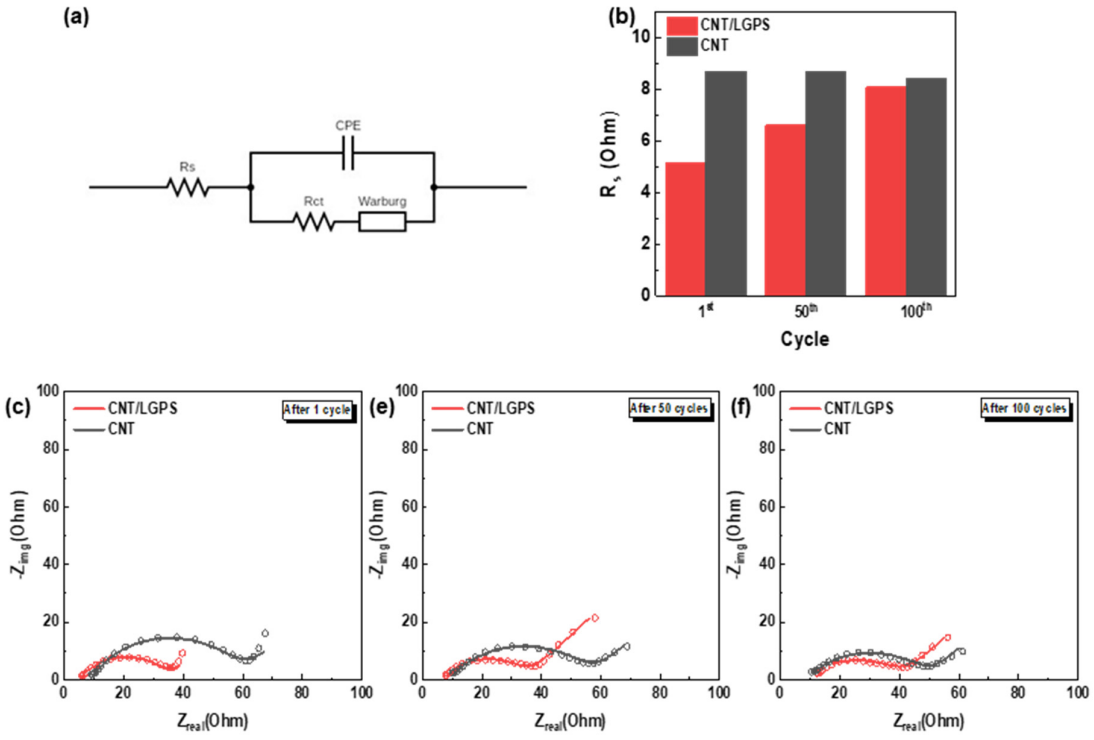

Figure S23. (a) The equivalent circuit model for analyzing EIS spectra. R_s, R_{ct}, Warburg, and CPE are denoted in the equivalent circuit as solution resistance, charge transfer resistance, Warburg impedance and constant phase elemental, respectively. (b) The comparison plots of R_s of CNT/LGPS and CNT. The fitted Nyquist plots after c) 1 cycle, e) 50 cycles, and f) 100 cycles. The cells were tested at 0.1 C using a sulfur loading of 4.6 mg cm^{-2} and an E/S ratio of 5.1 μL mg^{-1}. EIS was measured at a charged state (2.7 V vs. Li^+/Li).

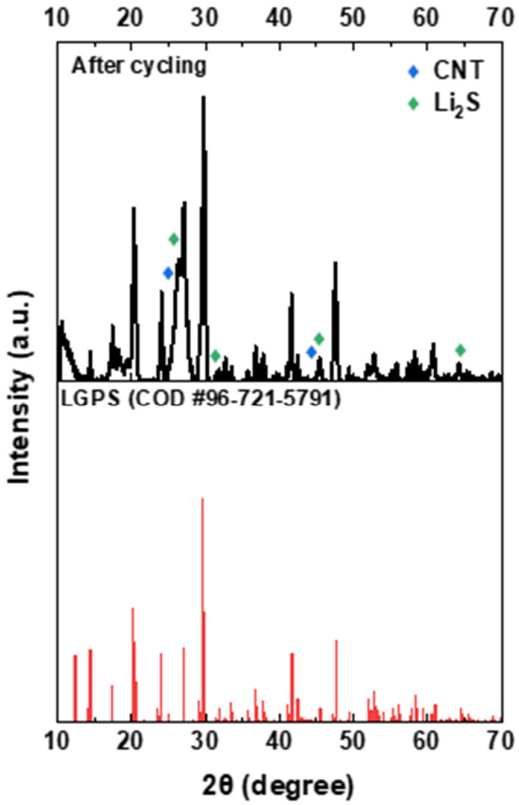

Figure S24. XRD spectra of CNT/LGPS electrodes after cycling with 6M catholyte.

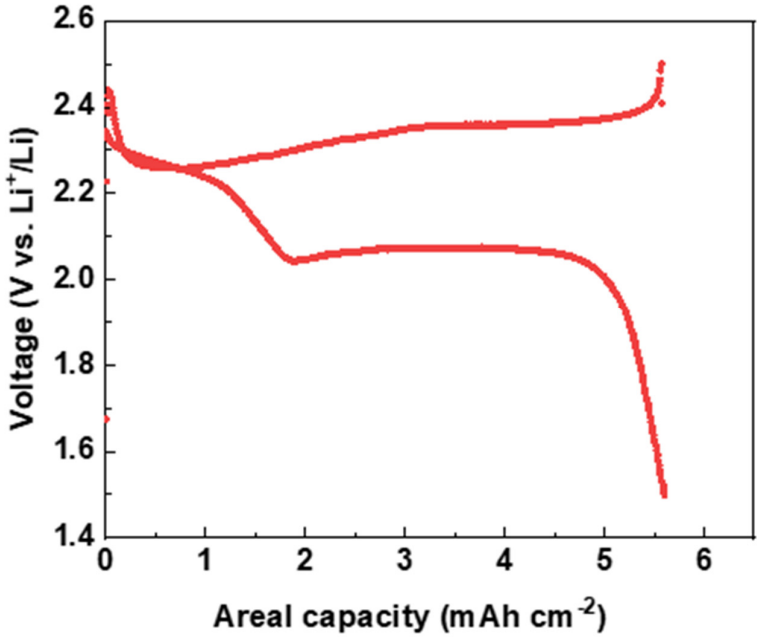

Figure S25. The representative charge/discharge profile of the 3rd cycle after activation of the LGPS cell at 0.05 C with a sulfur loading of 8.1 mg cm^{-2} and an E/S ratio of 2.9 µL mg^{-1}.

Table S5. The performance comparison under high sulfur loadings and low E/S ratios.

Materials	Function	E/S ratio [μL mg^{-1}]	Sulfur loading [mg cm^{-2}]	Current density [mA cm^{-2}]	Maximum areal capacity [mA h cm^{-2}]	Cycle life	Total energy throughput [mA h cm^{-2}]	Ref
CNT/LGPS	promoter	2.9	8.1	0.5	6.13	200	891	This work
CNT/LGPS	promoter	2.9	8.1	0.5	6.13	135	665	This work
MoP-CNT-10-S	electrocatalyst	4	6	0.8	5	50	249	[5]
S@CPZC	electrocatalyst	4.5	13.5	1.1	14.2	60	520	[6]
Ni-CF/S	electrocatalyst	5	5	0.84	4.5	150	556	[7]
CoNC@ Co_9S_8NC	electrocatalyst	4.5	8.8	0.74	9.5	50	341	[8]
MoS_{2-x}/rGO/S	electrocatalyst	5	5.6	0.5	5.6	100	488	[9]
NF@VG	electrocatalyst	4.8	10	1.7	11.2	100	973	[10]
NF@VG	electrocatalyst	4.8	13	2.2	12.8	100	1117	[10]
CoSe–ZnSe@G	electrocatalyst	3	7.7	0.26	8	40	177	[11]
NC@ Nb-TiO_{2-x}	electrocatalyst	4.5	6.5	2.2	4.43	100	400	[12]
rGO-$SmMn_2O_5$	electrocatalyst	4.6	5.6	1.9	5.04	200	750	[13]
S-FeN_2-NC	electrocatalyst	5.3	5	0.84	5.7	80	405	[14]
S/quasi-MOF NS	electrocatalyst	4.6	6.5	1.1	6.5	100	612	[15]
S/Fe-Co_3O_4 HHNPs	electrocatalyst	4.2	6.6	1.1	6.5	60	387	[16]
β–CD@CoPC	electrocatalyst	3.5	12.8	2.1	11.6	50	533	[17]
S/FeCo-SACC	electrocatalyst	4.6	15	2.5	10.2	50	449	[18]
DtbDS CoRM	mediator	5	5	1.7	3	50	132	[19]
DFAQ	mediator	5	5.8	0.97	9	80	559	[20]

NG-CN/CMC-CA	binder	3.5	10.2	1	11	50	350	[21]
S@DCP	binder	5	9.8	0.5	9	50	396	[22]
PEO_{10} LiTFSI	binder	3.3	4	0.8	4.8	100	360	[23]
0.5 M Li_2S_4	electrolyte	3	6.2	0.2	4.7	100	294	[24]
$LiNO_3$	electrolyte	5	4.5	0.38	5.4	75	379	[25]
50 vol% DMDS	electrolyte	5	4	0.2	5.2	25	104	[26]
SDHPC	cathode	2.8	8	0.34	10	20	126	[27]

Note S1. The detail calculation of the relative activation energy.

As shown in Figure 3a, CV tests were performed under a scan rate of 0.02 mV s^{-1} at 298K. The relationship between electrode potential and activation energy can be determined by equation (1) [28-31]:

$$E_a = E_a^0 + \alpha zF\varphi \tag{1}$$

where E_a is the activation energy of the reduction process; E_a^0 is the intrinsic activation energy; α represents the charge transfer coefficient; z represents the number of electrons involved; F represents Faraday constant; φ represents the peak potential of the reduction process in the CV curve.[30]

We can use Tafel plot to find the term, αzF in equation (1). The Butler-Volmer equation is as follow:

$$j = j_0(e^{\frac{(1-\alpha)zF\eta}{RT}} - e^{\frac{-\alpha zF\eta}{RT}}) \tag{2}$$

where j is the current density; j_0 is the exchange current density; R is the gas constant; T is the absolute temperature, η is the overpotential.

For the reduction reaction, assuming $\eta \ll 0$, the equation is simplified to:

$$|j_{cathode}| = j_0(e^{\frac{-\alpha zF\eta_{cathode}}{RT}}) \tag{3}$$

$$\frac{|j_{cathode}|}{j_0} = -e^{\frac{-\alpha zF\eta_{cathode}}{RT}} \tag{4}$$

$$\ln\left(\frac{|j_{cathode}|}{j_0}\right) = \frac{-\alpha zF\eta_{cathode}}{RT} \tag{5}$$

$$\eta_{cathode} = \frac{RT}{\alpha zF} ln j_0 - \frac{RT}{\alpha zF}|j_{cathode}| \tag{6}$$

The equation (6) is the well-known Tafel equation.

$$\eta_{cathode} = \frac{RT}{\alpha zF} ln\, j_0 - \frac{RT}{\alpha zF} ln\, j_{cathode} \quad (7)$$

$$\eta_{cathode} = a + b\, ln\, j_{cathode} \quad (8)$$

$$b = \frac{RT}{\alpha zF} \quad (9)$$

Where $\eta_{cathode}$ is the overpotential of the cathode; $j_{cathode}$ represents the current density of the cathode; *a* represents the intercept derived from the Tafel curve; *b* represents the slope of the Tafel curve. The equation (1) can be rewritten using *b* from the equation (9):

$$E_a = E^0{}_a - \frac{RT}{b}\varphi \quad (10)$$

According to the Tafel slope, the relative activation energy during the reduction process can be calculated. [30, 31]

The difference in activation energy corresponding to the reduction of S_8 to the high-order Li_2S_n:

CNT/LGPS ($\varphi = 2.25\ V$): $E_{a1} - E_{a1}^0 = -33.6$ kJ mol^{-1}

CNT ($\varphi = 2.15\ V$): $E_{a1} - E_{a1}^0 = -22.8$ kJ mol^{-1}

$\Delta E_{a1} = E_{a1(CNT/LGPS)} - E_{a1}^0 - \left(E_{a1(CNT)} - E_{a1}^0\right) = -10.8$ kJ mol^{-1}

The difference in activation energy corresponding to the reduction of Li_2S_n to the low-order Li_2S:

CNT/LGPS ($\varphi = 1.96\ V$): $E_{a2} - E_{a2}^0 = -23.3$ kJ mol^{-1}

CNT ($\varphi = 1.82\ V$): $E_{a2} - E_{a2}^{0} = -14.2$ kJ mol^{-1}

$\Delta E_{a2} = E_{a2(CNT/LGPS)} - E_{a2}^{0} - \left(E_{a2(CNT)} - E_{a2}^{0}\right) = -9.1$ kJ mol^{-1}

Note S2. The calculation of the gravimetric energy density.

$$E_g = \frac{V \times C}{m_{anode} + m_{cathode} + m_{current\ collector} + m_{seperator} + m_{electrolyte}}$$

E_g: Gravimetric energy density (Wh kg^{-1});

V: Average cell voltage (V);

C: Areal capacity (mAh cm^{-1});

m_{anode}: Areal mass of the anode calculated based on N/P ratio of 2 (mg cm^{-2});

$m_{cathode}$: Areal mass of the cathode (mg cm^{-2});

$m_{current\ collector}$: Total areal mass of the current collectors (Al: 2 mg cm^{-2}, Cu: 4 mg cm^{-2});

$m_{separator}$: Areal mass of the separator (1 mg cm^{-2});

$m_{electrolyte}$: Areal mass of the electrolyte

To calculate the gravimetric energy density of the cell with a E/S ratio of 2.9 μL mg^{-1}, we used C = 6.13 mAh cm^{-2} and V = 2.1 V. The areal mass of the Li metal anode was calculated when the N/P ratio ($R_{N/P}$) is 2 with the theoretical capacity of Li metal (C_{Li} = 3800 mAh g^{-1}).

$$m_{anode} = C \times R_{N/P} \div C_{Li} = \frac{6.13\ mAh}{cm^2} \times 2 \div \frac{3800\ mAh}{1000\ mg} = 3.2\ mg\ cm^{-2}$$

To calculate the areal mass of cathode, we considered the areal mass of CNT (m_{CNT}) and the areal mass of LGPS (m_{LGPS}).

$$m_{cathode} = m_{CNT} + m_{LGPS} = 7.2\ \text{mg}\ cm^{-2} + 1.5\ \text{mg}\ cm^{-2} = 8.7\ mg\ cm^{-2}$$

To calculate the areal mass of electrolyte, we used the sulfur loading (l_{sulfur}), the E/S ratio ($R_{E/S}$) of 2.9 μL mg^{-1}, and the amount of polysulfide was also considered. [3] The density of electrolyte (ρ_e) equals to 1.035 g cc^{-1}. So,

$$m_{electrolyte} = l_{sulfur} \times R_{E/S} \times \rho_e + l_{sulfur}$$

$$= 8.1\ mg\ cm^{-2} \times 2.9\ \mu l\ mg^{-1} \times 1.035\ g\ cc^{-1} + 8.1\ mg\ cm^{-2}$$

$$= 32.4\ mg\ cm^{-2}$$

$$E_g = \frac{V \times C}{m_{anode} + m_{cathode} + m_{current\ collector} + m_{seperator} + m_{electrolyte}}$$

$$= \frac{2.1\ V \times 6.13\ mAh\ cm^{-2}}{3.2\ mg\ cm^{-2} + 8.7\ mg\ cm^{-2} + 6\ mg\ cm^{-2} + 1\ mg\ cm^{-2} + 32.4\ mg\ cm^{-2}}$$

$$= 251\ Wh\ kg^{-1}$$

References

1. G. Yang, W. Choi, X. Pu and C. Yu, *Energy & Environmental Science*, 2015, **8**, 1799-1807.
2. G. Yang, J. Tan, H. Jin, Y. H. Kim, X. Yang, D. H. Son, S. Ahn, H. Zhou and C. Yu, *Advanced Functional Materials*, 2018, **28**, 1800595.
3. P. Wu, M. Dong, J. Tan, D. A. Kang and C. Yu, *Advanced Materials*, 2021, **33**, 2104246.
4. X. Liang, Q. Pang, I. R. Kochetkov, M. S. Sempere, H. Huang, X. Sun and L. F. Nazar, *Nature Energy*, 2017, **2**, 1-7.
5. Y. Yang, Y. Zhong, Q. Shi, Z. Wang, K. Sun and H. Wang, *Angewandte Chemie*, 2018, **130**, 15775-15778.
6. G. Li, W. Lei, D. Luo, Y. Deng, Z. Deng, D. Wang, A. Yu and Z. Chen, *Energy & Environmental Science*, 2018, **11**, 2372-2381.
7. Y. Tsao, H. Gong, S. Chen, G. Chen, Y. Liu, T. Z. Gao, Y. Cui and Z. Bao, *Advanced Energy Materials*, 2021, **11**, 2101449.
8. M. Zhen, K. Li and M. Liu, *Advanced Science*, 2023, **10**, 2207442.
9. H. Ye, J. Sun, X. F. Lim, Y. Zhao and J. Y. Lee, *Energy Storage Materials*, 2021, **38**, 338-343.
10. J. Lin, Y. Mo, S. Li and J. Yu, *Journal of Materials Chemistry A*, 2022, **10**, 690-698.
11. Z. Ye, Y. Jiang, T. Yang, L. Li, F. Wu and R. Chen, *Advanced Science*, 2022, **9**, 2103456.
12. Z. He, T. Wan, Y. Luo, G. Liu, L. Wu, F. Li, Z. Zhang, G. Li and Y. Zhang, *Chemical Engineering Journal*, 2022, **448**, 137656.
13. L. Wang, W. Hua, X. Wan, Z. Feng, Z. Hu, H. Li, J. Niu, L. Wang, A. Wang and J. Liu, *Advanced Materials*, 2022, **34**, 2110279.
14. J. Wang, W. Qiu, G. Li, J. Liu, D. Luo, Y. Zhang, Y. Zhao, G. Zhou, L. Shui and X. Wang, *Energy Storage Materials*, 2022, **46**, 269-277.
15. D. Luo, C. Li, Y. Zhang, Q. Ma, C. Ma, Y. Nie, M. Li, X. Weng, R. Huang and Y. Zhao, *Advanced Materials*, 2022, **34**, 2105541.
16. J. Liu, G. Li, D. Luo, J. Li, X. Zhang, Q. Li, H. Li, Y. Zhang and Z. Chen, *Advanced Functional Materials*, 2023, 2303357.
17. Y. Dong, H. Zhang, D. Cai, S. Yang, P. Ying, T. Li, J. Zou, M. Shu, R. Li and J. Wang, *Advanced Functional Materials*, 2024, 2406455.
18. X. Wang, X. Zhang, Y. Zhang, J. Wang, J. Liu, S. Li, X. Liu, M. Jin, L. Zhao and G. Li, *Advanced Energy Materials*, 2024, 2400926.
19. M. Zhao, B.-Q. Li, X. Chen, J. Xie, H. Yuan and J.-Q. Huang, *Chem*, 2020, **6**, 3297-3311.
20. W. Zhang, F. Ma, Q. Wu, Z. Cai, W. Zhong, Z. Zeng, S. Cheng and J. Xie, *ACS Applied Energy Materials*, 2022, **5**, 15719-15728.
21. Q. Pang, X. Liang, C. Y. Kwok, J. Kulisch and L. F. Nazar, *Advanced Energy Materials*, 2017, **7**, 1601630.

22. X. Liu, T. Qian, J. Liu, J. Tian, L. Zhang and C. Yan, *Small*, 2018, **14**, 1801536.

23. J. Chen, W. A. Henderson, H. Pan, B. R. Perdue, R. Cao, J. Z. Hu, C. Wan, K. S. Han, K. T. Mueller and J.-G. Zhang, *Nano letters*, 2017, **17**, 3061-3067.

24. H. Wang, Y. Shao, H. Pan, X. Feng, Y. Chen, Y.-S. Liu, E. D. Walter, M. H. Engelhard, K. S. Han and T. Deng, *Nano Energy*, 2020, **76**, 105041.

25. H. Chu, J. Jung, H. Noh, S. Yuk, J. Lee, J. H. Lee, J. Baek, Y. Roh, H. Kwon and D. Choi, *Advanced Energy Materials*, 2020, **10**, 2000493.

26. S. Chen, Y. Gao, Z. Yu, M. L. Gordin, J. Song and D. Wang, *Nano Energy*, 2017, **31**, 418-423.

27. M. Li, Y. Zhang, Z. Bai, W. W. Liu, T. Liu, J. Gim, G. Jiang, Y. Yuan, D. Luo and K. Feng, *Advanced Materials*, 2018, **30**, 1804271.

28. V. Protsenko and F. Danilov, *Journal of electroanalytical chemistry*, 2011, **651**, 105-110.

29. P. Rüetschi, *Journal of The Electrochemical Society*, 1959, **106**, 819.

30. X. Lin, W. Li, X. Pan, S. Wang and Z. Fan, *Batteries*, 2022, **9**, 14.

31. W. Hua, H. Li, C. Pei, J. Xia, Y. Sun, C. Zhang, W. Lv, Y. Tao, Y. Jiao and B. Zhang, *Advanced Materials*, 2021, **33**, 2101006.